# A MULTI-MATERIAL TOPOLOGY OPTIMIZATION APPROACH FOR LARGE-SCALE ADDITIVE MANUFACTURING OF NON-PERIODIC ARCHITECTED STRUCTURES

**Andrea Chiozzi [1], Andrea Nale [2], Fernando V. Senhora [3], Glaucio H. Paulino [4]**

[1] Department of Environmental and Prevention Sciences
University of Ferrara
C.so Ercole I d'Este, 32 - 44121 Ferrara, Italy
email: andrea.chiozzi@unife.it

[2] Department of Architecture
University of Ferrara
Via della Ghiara, 36, Ferrara 44121, Italy
email: andrea.nale@unife.it

[3] School of Civil and Environmental Engineering
Georgia Institute of Technology
790 Atlantic Drive NW, Atlanta, GA 30332, USA
email: fernandosenhora@gatech.edu@unife.it

[4] Department of Civil and Environmental Engineering
Princeton University
59 Olden St, Princeton, NJ 08540, USA
email: gpaulino@princeton.edu

**Key words:** multi-material optimization, large-scale additive manufacturing, non-periodic architected materials

**Summary.** Topology optimization algorithms allow the design of optimized structures under prescribed constraints, loads, and boundary conditions. In this contribution, a structural optimization framework is proposed to deal with the challenges posed by large-scale additive manufacturing. The formulation is a volume constrained compliance-based optimization, which leverages on the selection of suitable non-periodic architectures at the microscale, such as spinodal architected materials, by a multi-material and homogenization-based approach. The implemented architectures have unstructured and stochastic features, which are suitable for smooth transitions between different materials. The wide range of spinodal material classes achievable is combined with porosity and orientation setting, which provide high design freedom. The proposed approach is exemplified by exploiting the features of a novel large-scale water jetting powder-bed 3D printing technology.

# 1 INTRODUCTION

Topology optimization is a class of computational design tools that allows optimal distribution of material in a prescribed domain upon assigned boundary and loads conditions, while dealing with a target objective under constraints. Since its development, topology optimization has been mainly focused on theoretical aspects due to practical limitation in fabricating complex geometries. This shortcoming was overcome with the development of advanced manufacturing and 3D printing techniques, involving many engineering fields, such as automotive, aerospace, biomedical. Many manufacturing limits imposed by traditional manufacturing processes have been overcome by the development of technologies able to deal with scales ranging from nanometers to centimeters. The growth of additive manufacturing has recently become attractive also to the field of constructions. The need of new solutions is motivated mainly by the negative environmental impact of traditional manufacturing processes and the reduction of costs. Therefore, bridging topology optimization methods and additive manufacturing technology has become a particularly relevant challenge, in that it allows to minimize energy consumption and the carbon footprint. Indeed, topology optimization provides the optimal material distribution by efficiently reducing material usage with structures at "limits of economy" [1] while, on the other hand, additive manufacturing contributes to the reduction of material waste and $CO2$ emissions by allowing the use of alternative and eco-sustainable materials, such as natural and recycled raw aggregates combined with eco-friendly binders. Additionally, the advances on topology optimization and additive manufacturing motivated the community to investigate structural optimization problems at different scales. The control of microscale designs enables the definition of lightweight cellular solids with prescribed physical, mechanical and functional features at the macroscale. Despite the advantages, truss- and plate-based periodic microstructures suffer from stress concentrations at their members intersection with consequences on strength and reliability. An alternative is represented by triply periodic minimal surfaces (TPMS) [2], which avoids stress concentrations due to smooth topologies and leveraging on the benefits of doubly curved surfaces with an excellent scalability of structural properties. Most recently, stochastic non-periodic architectures obtained by mimicking spinodal decomposition in phase separation have attracted noticeable interest. Similarly to TPMS, spinodal architected materials present smooth and non-intersecting surfaces between different material classes [3]. In this contribution, we present a volume-constrained multi-material topology optimization formulation that maximizes the stiffness of the system, while handling optimal distribution of different classes of spinodal architectures, accounting for varying density and orientation [4]. The formulation is bridged with large-scale additive manufacturing by a voxel-based post-processing technique. The technology introduced additional restrictions on the formulation, such as domain definition and microstructural parameters setting, to take into account the nature and behavior of printed material, i.e. stone-like materials manufactured with specific aggregates and binders. We consider, in particular, structures that are self-supported, such as arches and vaults, to ensure prevailing compression stress states at the macroscale throughout the structure. As an example to illustrate the proposed approach we present the design of a catenary arch, a well-known architectural element characterized by the resultants of compression forces, i.e. the thrust line, entirely contained within the shape of the arch.

The paper is organized as follows: Section 2 details the topology optimization formulation, non-periodic architected materials and additive manufacturing technology, Section 3 outlines

numerical results and finally Section 4 provides conclusions and future perspectives.

## 2 MATERIALS AND METHODS

The proposed topology optimization formulation entails a multi-material approach based on homogenization, which allows to handle and include different microstructures in the iterative process. The problem is stated in Eq. 1, in which structural compliance, $J$, is minimized under volume constraints, $g_k$.

$$
\begin{aligned}
\min_{\mathbf{Z},\rho,\alpha,\beta,\gamma} \quad & J = \mathbf{F}^T\,\mathbf{U}(\mathbf{Z},\rho,\boldsymbol{\alpha},\boldsymbol{\beta},\boldsymbol{\gamma}), \\
\text{s.t.} \quad & g_k = \frac{\sum_{m\in\mathcal{G}_k}\sum_{\ell\in\mathcal{E}_j}A_\ell m_v(y_{\ell m})}{\sum_{\ell\in\mathcal{E}_k}A_\ell} - \overline{v}_k \le 0,\ k = 1,...,N^{\mathrm{c}}, \\
& Z_{\ell m} \in [0,1],\ \ell = 1,...,N^{\mathrm{el}},\ m = 1,...,N^{\mathrm{mat}}, \\
& \rho_\ell \in [\underline{\rho},\overline{\rho}],\ \{\alpha_{\ell m},\beta_{\ell m},\gamma_{\ell m}\} \in [-\pi,\pi], \\
\text{with} \quad & \mathbf{K}(\mathbf{Z},\rho,\boldsymbol{\alpha},\boldsymbol{\beta},\boldsymbol{\gamma})\,\mathbf{U}(\mathbf{Z},\rho,\boldsymbol{\alpha},\boldsymbol{\beta},\boldsymbol{\gamma}) = \mathbf{F},
\end{aligned}
\tag{1}
$$

The volume constraint has a flexible definition in order to set global or local material limitations. Local volume constraints are defined by material selection restriction on subdomains through index element lists. The material index list, $\mathcal{G}_k$, contains the material available in the optimization associated to element index list, $\mathcal{E}_k$, of the domain, in the case of global constraint, or sub-domains, in the case of local constraints. It is possible to assign, for design purposes, passive regions. These regions may be voids or made up of a specific material, which are respectively referred to as passive-void and passive-solid. The design variable space is composed by material existence, $\mathbf{Z}$, spinodal density, $\boldsymbol{\rho}$ in the manufacturability range (lower $\underline{\rho}$ and upper $\overline{\rho}$ bounds), and spinodal orientation angles, $\{\boldsymbol{\alpha},\boldsymbol{\beta},\boldsymbol{\gamma}\}$. The material design variable field, $\mathbf{Z}$, is regularized by a linear filter [5] assigning a radius that enforces the well-posedness of the problem and mesh-dependency of the discretized problem. The operator is coupled with a Heaviside projection [6] to encourage smooth transitions solid-void. The filtered density, $\tilde{Y}$ is finally penalized through a SIMP interpolation scheme [7] to remove intermediate densities. The material penalty $p$ and multi-material mixing $\tau$ factors are increased by a continuation scheme after reaching convergence or the maximum number of iterations. The factors are incremented until the desired penalty factor and the material mixing are reached. The solid boundaries of the optimal layout are suitably smoothed. A post-processing procedure is required to visualize and embed the implemented microstructual design. The domain is discretized into finite elements and a design variable space is associated to the discretized space. The displacement field, $\mathbf{U}$, is obtaining by solving the state equation of static elasticity $\mathbf{K}(\mathbf{Z},\rho,\boldsymbol{\alpha},\boldsymbol{\beta},\boldsymbol{\gamma})\,\mathbf{U}(\mathbf{Z},\rho,\boldsymbol{\alpha},\boldsymbol{\beta},\boldsymbol{\gamma}) = \mathbf{F}$. The design-independent nodal loads vector, $\mathbf{F}$, is assigned, while the global stiffness matrix, $\mathbf{K}$, is computed from the local element stiffness matrices [8] as follows:

$$
\mathbf{K}_\ell = \int_{\Omega_\ell}\mathbf{B}^T\mathbf{D}_\ell(\mathbf{Z}_\ell,\rho_\ell,\boldsymbol{\alpha}_\ell,\boldsymbol{\beta}_\ell,\boldsymbol{\gamma}_\ell)\mathbf{B}d\mathbf{x},,
\tag{2}
$$

The element-strain displacement matrix is $\mathbf{B}$ and the material matrix, $\mathbf{D}$, is calculated by multi-material interpolation of the $m$-candidate materials material matrix, $D_m^H$, according to:

$$\mathbf{D}_\ell = \sum_{m=1}^{N^m} w_{\ell m} \prod_{\substack{q=1 \\ q \neq m}}^{N^m} (1 - \tau w_{\ell q}) \mathbf{M}(\alpha_{\ell m}, \beta_{\ell m}, \gamma_{\ell m}) \mathbf{D}_m^H(\rho_\ell) \mathbf{M}^T(\alpha_{\ell m}, \beta_{\ell m}, \gamma_{\ell m}). \tag{3}$$

The optimal orientation of spinodal architectures reference frame is obtained by tensor transformation laws, $\mathbf{M}(\alpha_{\ell m}, \beta_{\ell m}, \gamma_{\ell m})$, for stress and strains. The angles $(\alpha_{\ell m}, \beta_{\ell m}, \gamma_{\ell m})$ are updated by Eq. 6. The $m$-candidate materials are included by a homogenized material elasticity tensor, $D_m^H$, calculated by classical homogenization theory [9] for assigned densities and topologies. The stochastic and non-periodic nature of spinodal topology is considered in the implementation by calculating the elastic tensor by means of 15 spinodal architectures. Each topology is calculated by applying level-set function to Eq. 11 and the computational homogenization is performed by discretizing the topology in 150x150x150 elements with Young's modulus, E = 1, and Poisson's ratio, $v = 0.3$ for the bulk material. The problem in Eq. (1) is solved by a gradient-based approach. The optimal solution is ruled by the sensitivities of objective and constraint functions with respect to design variables. The augmented lagrangian method [10] is adopted with the Steepest Descent Method (SDM) [11] to iteratively guide the design toward an optimal solution, a local minimum. The augmented lagrangian function is minimized in each inner iteration $t$ as the sum of objective function and the penalty term and reads:

$$\mathcal{L}(\mathbf{x})^{(\mathbf{t})} = J(\mathbf{x}) + \sum_{j=1}^K \left[ \lambda_j^{(t)} \max\left(g_j(x), -\frac{\lambda_j^{(t)}}{\mu^{(t)}}\right) + \frac{\mu^{(t)}}{2} max\left(g_j(x), -\frac{\lambda_j^{(t)}}{\mu^{(t)}}\right)^2 \right], \tag{4}$$

The penalization parameters, $\lambda_j^{(k)}$ and $\mu^{(k)}$, are updated every 5 outer iterations, $k$, as:

$$\lambda_j^{(k+1)} = \lambda_j^{(k)} + \mu^{(k)} \max\left(g_j^{(k)}(\mathbf{x}), -\frac{\lambda_j^{(t)}}{\mu^{(k)}}\right) \text{ and } \mu^{(k+1)} = 1.25\mu^{(k)}. \tag{5}$$

At each inner optimization iteration, $t$, the variables $\mathbf{x}$ are updates following the rule:

$$\mathbf{x}^{(t+1)} = \max\left[\min\left(\mathbf{x}^{(t)} - \tau^{(t)}\frac{\partial \mathcal{L}^{(t)}}{\partial \mathbf{x}}, \mathbf{x}^{(t)} + move\right), \mathbf{x}^{(t)} - move)\right], \tag{6}$$

where $move$ is move limit and $\tau^{(t+1)} = \max(0.99\tau^{(t)}, 0.01)$ is the step size with $\tau^{(0)} = 1$.
The sensitivities involved in the update scheme are the objective and penalty function and they are computed as follows:

$$\frac{\partial J}{\partial \mathbf{z}_m} = \frac{\partial y_{\ell m}}{\partial z_{\ell m}}\frac{\partial \tilde{y}_{\ell m}}{\partial y_{\ell m}}\frac{\partial J}{\partial w_{\ell m}}, \quad \frac{\partial J}{\partial \boldsymbol{\alpha}_m} = \frac{\partial J}{\partial \alpha_{\ell m}}, \frac{\partial J}{\partial \boldsymbol{\rho}} = \frac{\partial J}{\partial \rho_\ell}$$

$$\frac{\partial g_j}{\partial \mathbf{z}_m} = \frac{\partial y_{\ell m}}{\partial z_{\ell m}}\frac{\partial \tilde{y}_{\ell m}}{\partial y_{\ell m}}\frac{\partial v_{\ell m}}{\partial \tilde{y}_{\ell m}}\frac{\partial g_j}{\partial v_{\ell m}}, \quad \frac{\partial g_j}{\partial \boldsymbol{\rho}} = \frac{\partial v_{\ell m}}{\partial \rho_\ell}\frac{\partial g_j}{\partial v_{\ell m}}, \tag{7}$$

$$m = 1, ..., N^m, \quad j = 1, ..., N^c$$

where:

$$\frac{\partial y_m}{\partial Z_m} = \mathbf{P}^T, \frac{\partial w}{\partial \tilde{y}_{\ell m}} = p y_{\ell m}^{p-1}, \frac{\partial \tilde{y}}{\partial y_{\ell m}} = \frac{\xi(1 - \tanh^2(\xi(y_{\ell m} - \eta)))}{\tanh(\xi\eta) + \tanh(\xi(1 - \eta))},$$

$$\frac{\partial v_{\ell m}}{\partial \tilde{y}} = \rho_\ell, \frac{\partial v_{\ell m}}{\partial \rho_k} = \tilde{y}_{\ell m}, \frac{\partial g_j}{\partial v_{\ell m}} = \frac{V_\ell}{\sum_{\ell \in E_j} V_\ell} \tag{8}$$

The components of each objective and constraint sensitivities are defined as:

$$\frac{\partial J}{\partial w_{\ell m}} = -\mathbf{U}^T \frac{\partial \mathbf{K}}{\partial w_{\ell m}} \mathbf{U}, \;\; \frac{\partial J}{\partial \rho_\ell} = -\mathbf{U}^T \frac{\partial \mathbf{K}}{\partial \rho_\ell} \mathbf{U}, \; \frac{\partial J}{\partial \alpha_{\ell m}} = -\mathbf{U}^T \frac{\partial \mathbf{K}}{\partial \alpha_{\ell m}} \mathbf{U} \tag{9}$$

where the stiffness sensitivities are computed from the material elasticity tensor, with respect to the design variable, $\mathbf{w}$, the spinodal density, $\rho$, and the orientation angle ($\alpha$):

$$\frac{\partial \mathbf{D}_\ell}{\partial w_{\ell m}} = \prod_{\substack{q=1 \\ q \neq m}}^{N^m} (1 - \tau w_{\ell q}) \mathbf{M}_{\ell m} \mathbf{D}_m^H(\rho_\ell) \mathbf{M}_{\ell m}^T - \sum_{\substack{q=1 \\ q \neq m}}^{N^m} \gamma w_{\ell q} \prod_{\substack{r=1 \\ r \neq q \\ r \neq m}}^{N^m} (\tau_{\ell r}) \mathbf{M}_{\ell m} \mathbf{D}_m^H(\rho_\ell) \mathbf{M}_{\ell m}^T,$$

$$\frac{\partial \mathbf{D}_\ell}{\partial \rho_\ell} = \sum_{m=1}^{N^m} w_{\ell m} \prod_{\substack{q=1 \\ q \neq m}}^{m} (1 - \tau w_{\ell q}) \mathbf{M}_{\ell m} \frac{\partial \mathbf{D}_m^H(\rho_k)}{\partial \rho_\ell} \mathbf{M}_{\ell m}^T, \tag{10}$$

$$\frac{\partial \mathbf{D}_\ell}{\partial \alpha_{\ell m}} = \sum_{m=1}^{N^m} w_{\ell m} \prod_{\substack{q=1 \\ q \neq m}}^{N^m} (1 - \tau w_{\ell q}) \left[ \frac{\partial \mathbf{M}_{\ell m}}{\partial \alpha_{\ell m}} \mathbf{D}_m^H \mathbf{M}_{\ell m}^T + \mathbf{M}_k \mathbf{D}_m^H \frac{\partial \mathbf{M}_{\ell m}^T}{\partial \alpha_{\ell m}} \right]$$

with $\partial \mathbf{D}/\partial \beta_{\ell m}$ and $\partial \mathbf{D}/\partial \gamma_{\ell m}$ and of similar form.

The multi-material topology optimization formulation is bridged with a powder-bed water jetting additive manufacturing technique by a voxel-based strategy [12] to generate a readable file in Standard Triangulation Language .stl, as an input to the slicing software. The strategy enables the visualization of microstructural features and provides smooth continuity by entailing the optimized layout into homogeneous material regions. The design variables are projected into a finer grid and a discrete form of Eq. 11 is used to post-process the spinodal architectures.

In this work we employ a powder-bed water jetting technology that enables the production of large components. The printer is the Desa1 150.150, see Fig. 1, developed by Desamanera S.r.l. (Rovigo, Italy) [13]. The printer has a Cartesian gantry system allowing the production of a build volume of 1.5 m$^3$ with a square printing area of 1.5 m $\times$ 1.5 m. The system is composed of a frame of four columns and horizontal beams on the bottom and top. Each column is equipped with an electric motor that controls the vertical movement of the printer head. The horizontal beams provide stability. The printer head is composed of 264 nozzles placed in a straight line and separated according to a voxel dimension of 5.7 mm. The printer head is located on an intermediate beam crossing the printable area and connected to perpendicular double beams. The intermediate beam is carried through an electric motor controlling the planar movement. The layer thickness allowed has a range of 5-10 mm, while the voxel has dimensions spanning from 3 mm to 5.7 mm. These printer settings are defined by technical features of the system and design requirements of the object to be printed. The layer thickness and voxel dimensions in this work are set at 5.7 mm. The 3D model is pre-processed by a commercial 3D computer-aided design software. The object is imported into a in-house software and sliced into layers. The information, including opening and closing of nozzles, printing speed, voxel dimension, and layer thickness, are transmitted to the printer by an instruction code. The manufacturing process consists of repeated operations of laying and printing. The layer surface, i.e. the powder bed, is prepared by a recoater and a sand feeder after the material deposition. The flat surface is leveled according to the set layer thickness. The quality of the powder-bed is influenced by

the grain size of aggregates. In particular, the powder-bed is composed of natural aggregates and a magnesium-based binder. The voxel is activated by a water-admixture solution. The printed material is a magnesium-based cement and the object appears as a layered concrete structure. The non-activated powder acts as a support for the next layers, while formworks on the perimeter are employed to avoid movements of lower layers, e.g. horizontal translations caused by the weight of upper layers. Once the last layer is completed, the manufactured object is kept resting in the powder-bed to complete the material activation and guarantee an adequate layer adesion. The period elapsed between the printing and the post-processing is related to material formulation and object dimensions. The post-processing is structured in excavation and post-production treatments. The excavation, or extractions, is done by vacuum and tools. Then, air blowing removes the film of non-activated powders on the surface. Finally, a water treatment is applied to complete the chemical reaction of deeper parts The water bathing is repeated according to object size and the manufactured structure is dried at environmental conditions.

The powder-bed water jetting technology provides advantages in design freedom and materials flexibility. In addition, different aggregates are potentially implementable in the manufacturing process, e.g. marbles, stones, minerals, and other stone-like materials from recycled waste from the construction industry, according to grain size requirements and binder.



**Figure 1** Desa1 150.150 printer [13]

## 3   RESULTS AND DISCUSSION

The optimization problem stated in Eq. 1 is combined with a homogenization approach that enables the inclusion of microstructures to design hierarchical structures. The microstructural architectures implemented are spinodal architected materials. Their topologies stand on the thermodynamic concept of spinodal decomposition [14] where two phases spontaneously separate in an unstable phase that lies at maximum free energy. The random fluctuation in the concentration reduces the free energy of the system causing the spontaneous separation. The spinodal decomposition has been first modeled by the Cahn–Hilliard equation [15]. The computation is expensive and the control over the spinodal phase separation is limited. So, a phase field approximation has been proposed by a using a gaussian random field (GRF) [16].
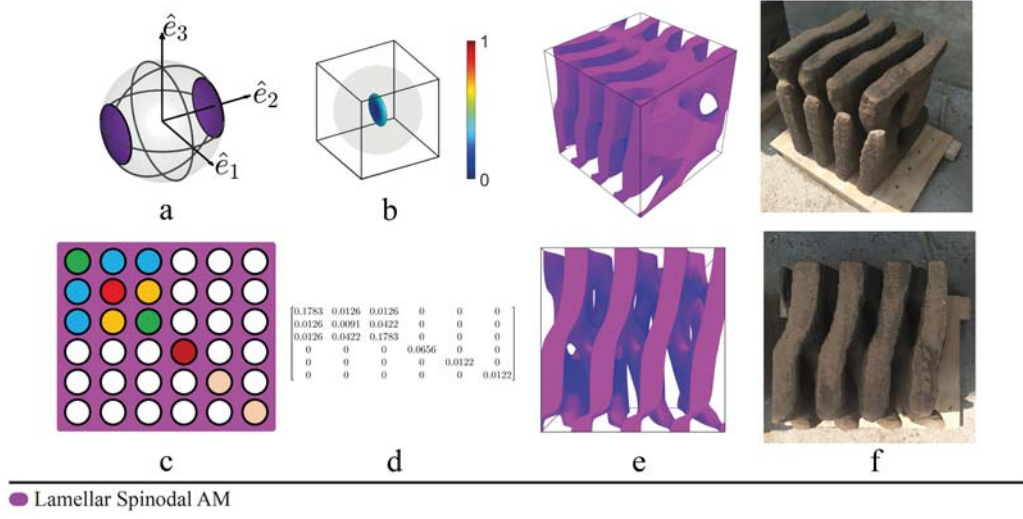
**Figure 2** Lamellar Spinodal Architected Material. a) wave vectors $\mathbf{n}_i$ space restricted by angles $\{(\theta_1, \theta_2, \theta_3) = (0, 30, 0)\}$, b) elastic surface with spinodal density $\rho = 0.4$. The gray volume is the elastic Voigt bound ($\rho E$) used as an upper bound. c) components of the homogenized stiffness elasticity matrix $D^H$, d) numerical values of $D^H$ model. Colors identifies values of the orthotropic material that are equal. The homogenized properties and the elastic surface are calculated on a Lamellar Spinodal Architected Material made of an elastic isotropic material with $E = 1$ Mpa and $\nu = 0$. A generic and planar view shows the e) numerical model and f) physical sample.

The introduction of a GRF, $\omega$, sets anisotropic features by manipulating the stochastic distribution of a set of wave vectors, $\mathbf{n}_i, i = 1, ... N^w$, on a unit sphere $\mathbf{n}_i \in \mathcal{U}[\mathbb{S}^2]$. The GRF in the Cartesian space $\mathbb{R}^3$ with basis $\{\hat{\mathbf{e}}_1, \hat{\mathbf{e}}_2, \hat{\mathbf{e}}_3\}$ is computed as follows:

$$\omega(\mathbf{x}) = \sqrt{\frac{2}{N^w}} \sum_{j=1}^{N^w} \cos \beta \mathbf{n}_j \cdot \mathbf{x} + \zeta_j, \tag{11}$$

with amplitude, $N^w$, wavelength, $\beta$ and phase shift $\zeta_j \in \mathcal{U}[0, 2\pi)$ of the $j$-th wave vector sampled as:

$$\mathbf{n}_j \in \mathcal{U}[\{\mathbf{m} \in \mathbb{S}^2 : (|\mathbf{m} \cdot \hat{\mathbf{e}}_1| > \cos \theta_1) \oplus (|\mathbf{m} \cdot \hat{\mathbf{e}}_2| > \cos \theta_2) \oplus (|\mathbf{m} \cdot \hat{\mathbf{e}}_3| > \cos \theta_3)\}], \tag{12}$$

where the angle set $\{\theta_1, \theta_2, \theta_3\} \in [0, \pi/2]$ restricts the wave vectors 12 on an unit sphere [16] providing the desirable anisotropic features.

The numerical model and the physical sample include the lamellar spinodal architecture. The lamellar class depicted in Fig, 2 is generated by restricting wave vectors through cone angles $\{\theta_1, \theta_2, \theta_3\} = \{0, 30, 0\}$.

The homogenized properties are included in the optimization formulation by the elastic matrix $D^H$. The manufactured sample, see Fig. 2.d, has been post-processed with wavelength $\beta = 25$, which fits the architected material with resolution requirements.
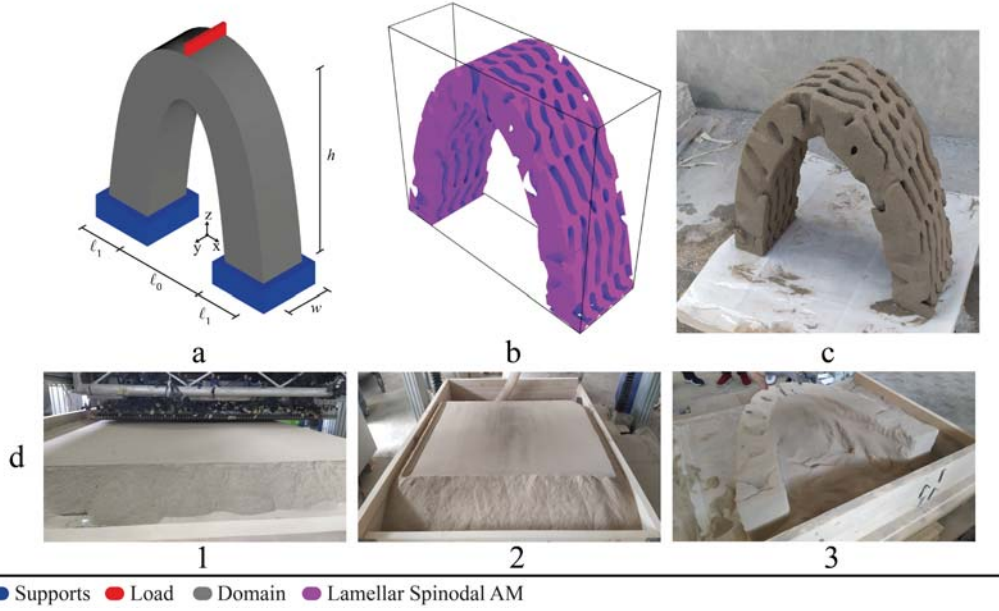
**Figure 3** Lamellar Catenary Arch: a) domain, b) numerical model, c) manufactured sample and d) printing and post-processing process. 1) laying operation, 2) printed object in the powder-bed completing the reaction and 3) excavation and object extraction.

The presented topology optimization formulation has been employed with a single candidate material, the lamellar class, with a global volume constraint $\overline{v}$. The optimization aims at optimally orienting the microstructure in the 3D space. The selected domain is a catenary arch with design and boundary conditions depicted in Fig. 3. The geometrical axis is defined by reversing the catenary equation $z = acosh(x \backslash a) = a(e^{x \backslash a} + e^{-x \backslash a}) \backslash 2$. The solid arch volume has been designed by setting the distance of the lowest point above the x axis, $a = 1/6$, and imposing constant depth along the axis, $\ell_1 = 15$ cm, with a span of $\ell_0 = 65$ cm. The overall length is $\ell = 95$ cm with an height of $h = 83$ cm and a width set as $w = 30$ cm.

The optimization is performed by initializing the design variable: material density $v_{lm} = \overline{v}/\rho_\ell$, $\forall_\ell$, density $\rho_\ell = (\underline{\rho} + \overline{\rho})/2$, $\forall_\ell$ and orientation $\alpha_\ell = 0, \beta_\ell = 0, \gamma_\ell = 0, \forall_\ell$. The material density is filtered by a linear filter with a given radius, $R = 0.4$. The design variables are updated with Eq. 6. The material density is updated at most with a $move_z = 0.1$, while orientation angles with $move_{ang} = 0.25$. The convergence is reached by evaluating the change in material density, **Z**, within a given tolerance, $tol$ and a maximum number of iterations $\max^{iter} = 150$ is set for each penalization step. The optimal solution is searched through a continuation penalization scheme with 5 penalization steps. The material penalty factor in the penalization steps is set $p = [1, 2, 2, 3, 4]$, while the multi-material interpolation parameter, $\tau$, is not required due to single-material optimization presented in this contribution. The iterative process optimizes the inner material distribution, porosity and orientation. The presented approach is tailored for a water jetting powder-bed additive manufacturing technology to manufacture self-supported structures due to printed material features, in which tensile strength properties are practically nonexistent. The numerical simulation and the physical sample demonstrate the applicability of a water-jetting powder-bed technology to print large-scale structures made of non-periodic

architected material.

## 4  CONCLUSIONS

The framework presented in this contribution outlines the scalability of spinodal architectures in a large-scale additive manufacturing framework by the manufacturing of a spinodal lamellar cube. The optimization and manufacturing of an optimally oriented lamellar catenary arch are presented in detail. The adopted topology optimization does not include any failure criterion. A formulation addressing practical application is a stress-based formulation [17], but its application with multiscale systems is currently challenging. The nature and behavior of stone-like materials with negligible tensile strength and the adopted topology optimization formulation have suggested to consider as an input design a self-supported structure, which is characterized by a prevailing compression stress state. Future challenges and outcomes will regard the investigation of the multi-material formulation presented with different classes with density ranges, considering both global and local volume constraints. In addition, the inclusion of a failure criterion represents a potential future development, i.e. stress-constraints formulation, that will extend the application of spinodal architected materials with topology optimization for practical applications in the field of civil engineering.

## REFERENCES

[1] Michell, A. G. M. (1904). The limits of economy of material in frame-structures. *The London, Edinburgh, and Dublin Philosophical Magazine and Journal of Science, 8(47), 589-597*

[2] Feng, J., Fu, J., Yao, X., & He, Y. (2022). Triply periodic minimal surface (TPMS) porous structures: from multi-scale design, precise additive manufacturing to multidisciplinary applications. *International Journal of Extreme Manufacturing, 4(2), 022001*

[3] Vidyasagar, A., Krödel, S., Kochmann, D. (2018). Microstructural patterns with tunable mechanical anisotropy obtained by simulating anisotropic spinodal decomposition. *Proceedings of the Royal Society A: Mathematical, Physical and Engineering Sciences, 474, 20180535*

[4] Sanders, E. D., Pereira, A., Aguiló, M. A., & Paulino, G. H. (2018). PolyMat: an efficient Matlab code for multi-material topology optimization. *Structural and Multidisciplinary Optimization, 58, 2727-2759*

[5] Bourdin, B. (2001). Filters in topology optimization. *International journal for numerical methods in engineering, 50(9), 2143-2158*

[6] Guest, J. K., Prévost, J. H., & Belytschko, T. (2004). Achieving minimum length scale in topology optimization using nodal design variables and projection functions. *International journal for numerical methods in engineering, 61(2), 238-254*

[7] Bendsøe, M. P. (1989). Optimal shape design as a material distribution problem. *Structural optimization, 1, 193-202*

[8] Bathe, K. J. (1996). Finite element procedures. *Klaus-Jurgen Bathe*

[9] Hassani, B., & Hinton, E. (2012). Homogenization and structural topology optimization: theory, practice and software. *Springer Science & Business Media*

[10] Nocedal, J., & Wright, S. J. (Eds.). (1999). Numerical optimization. *Springer New York*

[11] Bertsekas, D. P. (1997). Nonlinear programming. *Journal of the Operational Research Society, 48(3), 334-334*

[12] Senhora, F. V., Sanders, E. D., & Paulino, G. H. (2022). Optimally-tailored spinodal architected materials for multiscale design and manufacturing. *Advanced Materials, 34(26), 2109304*

[13] Desamanera. La stampa 3D dei Minerali per le grandi dimensioni. *www.desamanera.com*

[14] Binder, K. (1987). Theory of first-order phase transitions. *Reports on progress in physics, 50(7), 783*

[15] Cahn, J. W., & Hilliard, J. E. (1958). Free energy of a nonuniform system. I. Interfacial free energy. *The Journal of chemical physics, 28(2), 258-267*

[16] Portela, C. M. (2019). Fabrication, Mechanical Characterization, and Modeling of 3D Architected Materials Upon Static and Dynamic Loading. *California Institute of Technology*

[17] Senhora, F. V., Giraldo-Londono, O., Menezes, I. F., & Paulino, G. H. (2020). Topology optimization with local stress constraints: a stress aggregation-free approach. *Structural and Multidisciplinary Optimization, 62, 1639-1668*